Predictive-Quality Surface Reaction Chemistry in Real Reactor Models: Integrating First-Principles Kinetic Monte Carlo Simulations into Computational Fluid Dynamics

Sebastian Matera,*[,†,§] Matteo Maestri,*[,‡] Alberto Cuoci,[‖] and Karsten Reuter[†]

[†]Chair for Theoretical Chemistry and Catalysis Research Center, Technische Universität München, Lichtenbergstrasse 4, D-85747 Garching, Germany

[‡]Laboratory of Catalysis and Catalytic Processes, Dipartimento di Energia, Politecnico di Milano, P.zza Leonardo da Vinci 32, I-20133 Milano, Italy

[‖]Dipartimento di Chimica, Materiali e Ingegneria Chimica, Politecnico di Milano, P.zza Leonardo da Vinci 32, I-20133 Milano, Italy

1. INTRODUCTION

The observable (and exploitable) functionality of heterogeneous catalysts results from the interplay of two quite distinct aspects.[1] On the one hand, there are the intrinsic catalytic properties of the active catalyst material when interacting with molecules of the surrounding gas phase. They derive from the material's property to make and break chemical bonds at its surface(s) and are ultimately determined at the electronic structure level. On the other hand, there is the macroscopic heat and mass flow in the actual reactor geometry and at the actually employed operation conditions, which determines the local gas-phase concentrations and temperature at the catalyst surface. Both aspects are generally intricately coupled. The surface structure and composition of the catalyst (and therewith its intrinsic catalytic properties) depend sensitively on the local gas-phase conditions, i.e. the catalyst adapts to the reaction conditions and the ultimate "active phase" is a sensitive function of the local environment while on stream. Vice versa, the ongoing surface chemical conversions and the concomitant reaction heat modify this local environment and therewith contribute to the establishing flow patterns in the reactor.

Traditionally, one each aspect has been worked on by two quite distinct communities. Chemical engineering work focused primarily on the reactor level; fundamental surface science focused primarily on the reactive surface chemistry. In computational work, this has, on the one hand, led to the development of most powerful computational fluid dynamics (CFD) simulation approaches.[2] They are capable of describing the heat and mass flow in realistic reactor models, but they rely on simplified reaction kinetic expressions such as generic power laws that lack any surface chemical basis. The counterparts in surface science are increasingly detailed microkinetic descriptions, largely developed for controlled experiments, e.g. in ultrahigh vacuum (UHV), where heat and mass-transfer effects in a given reactor geometry are negligible.[3] In particular, first-principles kinetic Monte Carlo (1p-kMC) simulations fully resolve spatial heterogeneities and site correlations at the catalyst surface, while drawing on kinetic parameters for the elementary processes from quantitative first-principles calculations.[4]

Recent years have seen a merging of these two strands at an amazing pace. Chemical engineers introduce increasingly

Received: August 8, 2014
Revised: October 2, 2014

refined kinetic expressions into their reactor models, which at the CFD level of theory enter in the form of boundary conditions for the macroscopic fields. Noteworthy, the CatalyticFoam solver[5] exploits the operator-splitting technique to separate transport and reaction terms, and therewith allows already for the solution of the Navier−Stokes equations for complex and general flows at reactive surfaces described on the level of mean-field microkinetic rate equations. The CatalyticFoam solver is intrinsically dynamic, and the steady state is reached by time-dependent simulation. In this respect the separation between reaction and flow-time scales is essential. This feature is extremely important when multiple steady-state solutions are possible depending on the initial conditions.[5] In particular within the notion to establish so-called *in situ* approaches dealing with model catalysts at near-ambient operation conditions, kinetic modelers in turn care increasingly about heat and mass transport effects and integrate their kinetic descriptions into successively refined reactor models. In particular, Matera and Reuter employed an instantaneous steady-state approximation to generically present any irregularly gridded steady-state reactivity data of any complex (first-principles) kinetic model in the form of an interpolated data field for the boundary condition.[6,7]

In their original work, Matera and Reuter presented this for idealized reactor geometries.[6−8] Conceptually, however, nothing prevents this approach from being employed in more powerful general solvers such as CatalyticFoam, as long as one maintains the assumption that the length scales of temperature and pressure variations at the catalyst surface are large compared to the correlation lengths of the adsorbate populations. Under this assumption, which is also the general framework for most CFD simulations based on more coarse-grained kinetic expressions,[2] the intrinsic catalytic activity at every resolved surface mesh point of the macroscopic fields is solely dependent on the local temperature and partial pressures at this point. The activity at neighboring mesh points only enters indirectly through its effect on these local gas-phase conditions, not directly through some coupling mediated by the surface population itself. In particular for macroscopically homogeneous catalysts, such as the single-crystal model catalyst surfaces used to illustrate the approach in this work, it then suffices to determine one interpolated data field for the intrinsic catalytic activity as a continuous function of the temperature and all partial pressures. This data field can then be used as a CFD boundary condition independently at every CFD surface mesh point.

In this paper we contribute to this general context by augmenting the CatalyticFoam functionality to consider such interpolated data fields as the reactive surface boundary condition. In this endeavor to make complex kinetics available for practitioners in general CFD solvers an important intermediate step is hereby to optimize the reliability and efficiency with which such an interpolated representation can be generated from gridded activity data, e.g. from 1p-kMC simulations. To this end, our work includes a refined modified Sheppard interpolation approach, which allows faithful representation of the abrupt activity changes over a narrow range of gas-phase conditions, as typically obtained in 1p-kMC based kinetics with a limited number of grid data points. In the following we describe this interpolation strategy and the CatalyticFoam implementation after a brief survey of the general theory. We demonstrate the capabilities of the established approach by applying it to a series of problems of increasing flow complexity that are particularly geared toward *in situ* experiments at flat-faced model catalysts. In all cases we do observe intricate couplings of reactive surface chemistry and flow that significantly modify the observable catalytic function. This underlines the necessity of reliable accounts of both aspects in integrated multiscale catalysis simulations when aiming to establish an atomic-scale mechanistic understanding of this function in technologically relevant environments.

2. METHODOLOGY

2.1. Continuum Transport Equations. CFD packages such as CatalyticFoam[5] evaluate the macroscopic flow of heat and mass in a given reactor geometry by numerically solving continuum conservation equations for mass, energy, and momentum of a multicomponent, compressible gas phase. For a Newtonian fluid, these equations of total mass, mixture momentum, individual species mass fractions, and mixture energy, respectively, read as follows:[9]

$$\frac{\partial \rho}{\partial t} + \nabla\cdot(\rho \underline{v}) = 0 \tag{1}$$

$$\frac{\partial}{\partial t}(\rho \underline{v}) + \nabla\cdot(\rho \underline{v}\,\underline{v}) + \nabla\left(p + \frac{2}{3}\mu\nabla\cdot\underline{v}\right) - \nabla\cdot\mu(\nabla \underline{v} + \nabla \underline{v}^T) = \rho \underline{g} \tag{2}$$

$$\frac{\partial}{\partial t}(\rho\omega_k) + \nabla\cdot\rho\omega_k\underline{v} + \nabla\cdot(\rho\omega_k\underline{V}_k) = \tau^\alpha \tag{3}$$

$$\rho c_p\frac{\partial T}{\partial t} + \rho c_p \underline{v}\nabla T - \nabla\cdot(\lambda\nabla T) = -\sum_{k=1}^{N_g}\rho c_{p,k}\omega_k\underline{V}_k\cdot\nabla T - \sum_{k=1}^{N_g} H_k\tau_k \tag{4}$$

In these equations, t is the time, p and T are the total pressure and the temperature, respectively, ρ is the density, λ is the thermal conductivity, μ is the dynamic viscosity, and c_p is the specific heat at constant pressure of the gas-phase mixture. $\underline{v}$ is the velocity vector and $\underline{g}$ the acceleration vector due to gravity. N_g is the number of different species in the multicomponent gas mixture. The subscript k refers to the individual gas-phase species k, and ω_k is its mass fraction. $\underline{V}_k$ is its diffusion velocity, τ_k its formation rate due to the gas-phase reactions, $c_{p,k}$ its specific heat at constant pressure, and h_k its mass specific enthalpy in the gas phase.

The density of the mixture is calculated using the equation of state for ideal gases. As we are considering low fluid velocities, we employ the Low Mach Number Approximation to filter out acoustic (high frequency) modes in the compressible Navier−Stokes equations, which allows significantly larger time steps in the numerical solution. For this we decompose the total pressure into a spatially constant component from which we calculate the density and the so-called dynamic pressure, which appears only in the momentum balance.[7] Both Fickian and thermal diffusion are taken into account for evaluating the diffusion velocities, according to the approach suggested in[10]

$$\underline{V}_k = -\frac{\Gamma_k}{\omega_k}\nabla\omega_k - \frac{\Gamma_k\theta_k}{TX_k}\nabla T \tag{5}$$

where Γ_k is the individual species mixture averaged diffusion coefficient, X_k the mole fraction, and θ_k the thermal diffusion ratio. Mass conservation is enforced by employing the approach proposed in ref 11, based on the definition of a conservation diffusion velocity. In particular, in this approach a corrected diffusion velocity vector $\underline{V}_k^C$ is used in eqs 3 and 4 instead of $\underline{V}_k$. This vector is given as

$$\underline{V}_k^C = \underline{V}_k + \underline{V}_C \tag{6}$$

where $\underline{V}_C = -\sum_{k=1}^{Ng} \omega_k \underline{V}_k$ is a constant correction factor (independent of species, but varying in space and time) introduced to satisfy the mass conservation. The evaluation of transport properties is performed through mixture averaging rules, with the actual pure species transport and thermochemical coefficients calculated as described in detail in ref 7.

2.2. Boundary Conditions. For the solution of the above conservation equations, boundary conditions are required for all dependent fields, i.e. total pressure, velocity vector, species mass fractions, and temperature. Equivalently, velocity vector, temperature, and all partial pressures $\{p_k\}$ could be specified. In the present context of catalytic reactors, the boundary conditions for the total pressure are generally imposed in the form of a fixed pressure value at the outlet boundary and a zero-gradient condition at the inlet and at the reactor walls. For the velocity field, no-slip conditions are assumed at the walls; that is, the tangential components are set to zero there. We further assume that no mass accumulates on the surfaces, which is justified by the vanishing volume of the surface region. This results in a zero normal velocity component to respect mass conservation. At the inlet the velocity profile is assigned, while at the outlet boundaries the flow is assumed to be fully developed and a zero normal gradient is imposed.

The boundary conditions for the gas-phase species mass fractions (or partial pressures) and temperature at the inlet result from the feed conditions that are to be simulated. As such, the temperature is simply set to a prescribed value. For the gas-phase species, Danckwerts' conditions are instead imposed; that is, the total mass flux for each species k (accounting for diffusion and convection) is specified. If composition gradients exist at the boundary, these conditions allow diffusion into the computational domain and, therefore, give a more accurate description than classic Dirichlet conditions

$$\rho\omega_k(\underline{v} + \underline{V}_k)\cdot\underline{n} = (\rho\omega_k\underline{v})_0\cdot\underline{n} \tag{7}$$

where the term on the right side is the prescribed total mass flux and $\underline{n}$ is the inward pointing normal vector.

The reactor outlet boundaries are usually far enough downstream, so that temperature and concentration gradients have vanished and a zero normal gradient for T and ω_k can be assumed. At inert reactor walls, the normal mass flux of the individual species k must be equal to zero, as no species are consumed or produced. To leading order, this corresponds to a zero normal gradient for the mass fractions. If the inert walls are assumed adiabatic, i.e. heat dissipation through them is neglected, the normal gradient of the temperature is equally set to zero. Else, a Dirichlet boundary condition for T is imposed; that is, the temperature is fixed to a given value (which still might vary spatially and temporally though).

At catalytically active walls, i.e. the actual catalyst surface, the mass flux of the individual species k must balance with the formation rate (mass source) τ_k^{het} due to the ongoing heterogeneous reactions

$$\rho\omega_k\underline{V}_k\cdot\underline{n} = \tau_k^{het} = \sum_{\alpha}^{N^{het}} \nu_{\alpha,k} m_k R_\alpha^{het} \tag{8}$$

where $\underline{n}$ is again the inward pointing normal vector. R_α^{het} are the reaction rates (measured as turnover-frequency (TOF) in a number of reactions per unit time and surface area) of the N^{het} different ongoing surface reactions, $\nu_{\alpha,k}$ is the stoichiometric coefficient of species k in reaction α, and m_k is the molecular mass of species k.

Analogously, the (intrinsic) heat flux $-\lambda\nabla T$ must balance with the heat Q^{het} released by the heterogeneous reactions occurring on the catalytically active wall and with the heat flux $\underline{q}^{solid}$ in the solid bulk of the catalyst

$$\lambda\nabla T\cdot\underline{n} = Q^{het} - \underline{q}^{solid}\cdot\underline{n} \tag{9}$$

If the temperature of the catalyst surface can be controlled to a given value (e.g., through external heating), the above formula is replaced with the corresponding Dirichlet boundary conditions. Adiabatic operation, i.e. no heat dissipation into the solid, results from setting the solid heat flux to zero.

2.3. Integrated Surface Chemistry and Instantaneous Steady-State Approximation. The reactive surface chemistry enters the partial differential equations describing the flow through the boundary conditions for the mass flux, eq 8, and the heat flux, eq 9, at the catalytically active walls. This leads generally to the aforementioned intricate coupling of both aspects. On the one hand, the gas-phase species concentration profiles and temperature at the catalyst surface are modified by the actual catalytic activity, τ_k^{het}. On the other hand, this activity is, of course, a sensitive function of the local gas-phase conditions, i.e. the values of these fields at the surface. If the reaction rate is determined from simple phenomenological mean-field microkinetics, this coupling can be explicitly addressed. The corresponding rate equations can be efficiently incorporated into the actual CFD, e.g. by operator splitting techniques, as proposed by Maestri and Cuoci.[5] For more demanding microkinetic models, a corresponding direct integration may nevertheless quickly become the numerical bottleneck. This holds even more for a kMC-based description of the catalytic activity, where additional potential instabilities have hitherto restricted the direct coupling approach to very simple flow geometries and surface models.[12−15]

An appealing alternative is therefore to achieve an effective decoupling of the problem through an instantaneous steady-state approximation.[2,7] This approximation exploits the typically quite different time scales of surface kinetics and gas flow. Upon a change of the local gas-phase conditions (temperature, pressure, species mass fractions), the surface relaxes to a new steady-state catalytic activity corresponding to these changed conditions on time scales that are generally much shorter than those on which changes in the macroscopic fields actually occur. If this steady state is unique, there is then no need to actually evaluate the coupled dynamics of surface chemistry and flow fields. Instead, for whatever dynamical change of the flow field, the surface kinetics can thus be assumed to adapt instantaneously, and the reaction rates required for the boundary conditions in eqs 8 and 9 can at each time be replaced by the steady-state reaction rates for the current gas-phase conditions.

Under this approximation it thus suffices to have a continuous representation of the steady-state reaction rates as a function of the gas-phase conditions (temperature, pressure, species mass fractions or equivalently temperature, partial pressures). Only this representation is employed in the evaluation of the CFD boundary conditions; that is, the factor determining the overall computational efficiency is the efficiency with which this representation can be evaluated and not necessarily the efficiency with which the actually employed kinetic model yields the steady-state reaction rates. If the latter is numerically demanding, or as in the case of kMC simulations yields the steady-state reaction rates only in the form of discrete data, then the steady-state reaction rates can be precomputed once before the CFD simulation and be used to determine a numerically efficient continuous representation, e.g. through interpolation (*vide infra*).

We have to mention that the current approach (both for the model of the reaction rates as well as for employed boundary conditions) relies on the neglect of any direct communication between macroscopic points; that is, these points affect each other only by the transport in the bulk phases. This is a common approximation in the modeling of catalytic flows, which[2] is justified by the reaction conditions varying over length scales which are several orders of magnitude larger than the characteristic lengths of the surface kinetics. The concomitant transport on the surface is then sufficiently small that it is negligible compared to the gas surface interaction. On these length scales, the reaction conditions can therefore be considered homogeneous and nonlocal effects can be neglected. For more extreme situations, this needs not be the case, e.g. for microscopic flows with concomitant large concentration gradients. However, there the use of continuum mechanics to model the gas flow is at least questionable, as the characteristic system size approaches the mean free path in the gas.

2.4. First-Principles Kinetic Monte Carlo Simulations. In this work, the surface kinetics are derived from 1p-kMC simulations.[4,16] As with any microkinetic approach, the molecular-level basis of 1p-kMC simulations is all elementary processes involved in the catalytic cycle and their corresponding rate constants. In the 1p-kMC approach employed here, these rate constants are obtained from density-functional theory (DFT) calculations together with harmonic transition state theory (hTST).[17] On this basis, the actual 1p-kMC simulation achieves a numerical solution of the Markovian master equation describing the rare-event type time evolution of the surface system.

In order to keep the required first-principles input tractable, prevalent 1p-kMC realizations focus on a coarse-grained lattice representation of the surface system consisting of the individual active sites.[18] In contrast to prevalent rate-equation based microkinetic theory, which only achieves a mean-field approximate solution of the Markovian master equation, 1p-kMC simulations fully account for all lateral and temporal correlations and fluctuations in the occupation of these lattice sites with surface species.[19,20] Through the temperature and pressure dependence of the rate constants, the solution of the master equation depends parametrically on these. After suitable statistical or time averaging, the central outcome of a 1p-kMC simulation in the present context is thus the steady-state catalytic TOFs R_α^{het} of all surface reactions α for given temperature and partial pressures.

Through 1p-kMC simulations for a wide range of temperature and partial pressure conditions, one generates the data points that after suitable interpolations into a continuous representation serve for the boundary conditions, eqs 8 and 9, in the CFD simulations. These representations, $R_\alpha^{\mathrm{het}}(T,\{p_k\})$, $k = 1, ..., N_g$, henceforth called TOF-maps, generally feature largely exponential dependencies on partial pressures and an inverse dependence on temperature in large portions of $(T, \{p_k\})$-space.[21] These regions correspond to stable "phases" with defined surface coverages, and high catalytic activity is typically narrowly confined to conditions representing boundaries of these "phases".[22,23] In contrast to mean-field microkinetic models which tend to smear out these "phase" transitions, 1p-kMC simulations characteristically feature large variations in TOFs over a particularly small range of temperature and partial pressures. This challenges any interpolation approach of the $(N_g + 1)$-dimensional data field and motivates the specifics of the error-based modified Shepard approach introduced below. In practice, we also found it numerically convenient to rather interpolate the logarithm of the reaction rates as a function of the logarithms of the partial pressures and the inverse temperature. More precisely, we thus interpolate the function

$$\log_{10}(R_\alpha^{\mathrm{het}}) = f(\{x_{p_k}\}, x_T) \tag{10}$$

with

$$x_{p_k} = \frac{1}{a_k}\log_{10}(p_k) \quad \text{and} \quad x_T = \frac{1}{b_T}\frac{1}{T}$$

where coefficients a_k and b_T are chosen such that the features of the function $f(\{x_{pk}\},x_T)$ have a similar resolution in all independent directions. This particular choice of functional dependence leads to an almost linear behavior in the regions of $(T,\{p_k\})$-space corresponding to "stable" phases.[21] These regions can then be interpolated with a minimum of data points, when employing a method which uses local polynomials for interpolation.

2.5. Error-Based Modified Shepard Interpolation. Written more generally, the interpolation task can be stated as the generation of an interpolant $S(\mathbf{X})$ of a function $f(\mathbf{X})$, with $X = \{\{x_{pk}\},x_T\}$ on a $D = (N_g+1)$-dimensional domain Ω, based on N interpolation points $\mathbf{X}_j$ and the function values f_j, at these points. The basic idea of the modified Shepard interpolation approach[24] is to construct an approximate Taylor expansion $Q_j(\mathbf{X})$ at each interpolation point $\mathbf{X}_j$

$$Q_j(\mathbf{X}) = f_j + \sum_{a=1}^{D}\left(\frac{\partial f}{\partial X_a}\right)(\mathbf{X}_j)\Delta X_{j,a}... \tag{11}$$

where $\Delta X_{j,a} = X_a - X_{j,a}$. In the absence of derivative information at the interpolation points, the polynomial $Q_j(\mathbf{X})$ is fitted to the N_q nearest neighbor nodes of the node j in the weighted least-squares sense. The weight for each neighboring node i is hereby the inverse square distance $1/\|\mathbf{X}_j - \mathbf{X}_i\|^2$, where $\|\cdot\|$ is the euclidean norm. The function value f_j itself is not fitted so that the interpolation constraint $Q_j(\mathbf{X}_j) = f_j$ is automatically fulfilled. The continuous representation $f(\mathbf{X})$ of the original data field $f(\mathbf{X}_j)$ is then a superposition of the local Taylor polynomials

$$f(\mathbf{X}) = \sum_{j=1}^{N} Q_j(\mathbf{X})W_j(\mathbf{X}) \tag{12}$$

with $W_j(\mathbf{X})$ being a Shepard partition of unity, i.e. $W_j(\mathbf{X}) \geq 0$, $\sum_j W_j(\mathbf{X}) = 1$, and $W_j(\mathbf{X}_l) = \delta_{jl}$. In this way, the necessary interpolation property $S(\mathbf{X}_j) = f(\mathbf{X}_j)$ is again ensured.[25]

In order to obtain a local formulation, the weights $W_j(\mathbf{X})$ take the form

$$W_j(\mathbf{X}) = \frac{w_j(\mathbf{X})}{\sum_{l=1}^{N} w_l(\mathbf{X})} \quad \text{with} \quad w_j(\mathbf{X}) = \frac{\varsigma_j(\mathbf{X})}{\upsilon_j(\mathbf{X})} \tag{13}$$

where $\upsilon_j(\mathbf{X}) > 0$ tends to zero as $\mathbf{X}$ approaches $\mathbf{X}_j$ and increases as distance increases. The localization function $\varsigma_j(\mathbf{X})$ in turn is nonzero only inside a small cloud ω_j around the node j. The time for the evaluation of the interpolant S can thus be made sublinear in the number of data points N, as only a small fraction of the nodes have a nonzero contribution in the sum in eq 12. To obtain Renka's classical method, one chooses $\upsilon_j(\mathbf{X}) = 1/\|\mathbf{X} - \mathbf{X}_j\|^2$ and $\zeta_j(\mathbf{X}) = (R_j - \|\mathbf{X} - \mathbf{X}_j\|)_+^2$, where the + indicates that the brackets return zero if the content is negative. The radius R_j of the cloud ω_j is chosen such that the N_w nearest neighbors are included in the cloud. An alternative is, for example, implemented in the ALGLIB library[26]

$$\varsigma_j(\mathbf{X}) = (R(\mathbf{X}) - |\mathbf{X} - \mathbf{X}_j|)_+^2 \tag{14}$$

The difference to Renka's method is that the radius $R(\mathbf{X})$ is now the maximum distance of the N_w nearest neighbors of the query point $\mathbf{X}$ and not of node j. The cloud ω_j is thus implicitly defined by all points for which the node j is among the N_w nearest neighbors. The advantages are 2-fold: (i) the weights W_j are now guaranteed to be defined on the whole domain Ω, regardless of the distribution of the data points and (ii) the search for the nonzero contributions can efficiently be performed using kd-trees, even for inhomogeneously distributed data.

In the above approaches, the weight of the polynomial $Q_j(\mathbf{X})$ is solely determined by the distance of its node to the query point $\mathbf{X}$. This approach has limitations for functions that exhibit rapid changes of the local gradient over distances comparable to the local resolution of nodes, which is a situation typically encountered for 1p-kMC based TOF-maps with their rapid activity changes in "phase" boundary regions. In such situations, it might well happen that a polynomial belonging to a more distant node actually approximates the behavior at the query point much better than those polynomials belonging to close by nodes. This is illustrated in Figure 1 and motivates us to use weights that are not distance, but approximation-error based. We correspondingly choose

$$u_i(\mathbf{X}) = 1/\epsilon_j(\mathbf{X}) \tag{15}$$

where $\epsilon_j(\mathbf{X})$ is an error bound for the Taylor polynomial $Q_j(\mathbf{X})$, i.e.

$$\epsilon_j(\mathbf{X}) \geq |Q_j(\mathbf{X}) - f(\mathbf{X})|, \quad \forall\, \mathbf{X} \in \omega_j \tag{16}$$

For the localization function we choose

$$\varsigma_j(\mathbf{X}) = \begin{cases} 1 & ,x = S^D\left(\dfrac{(R - \|\mathbf{X} - \mathbf{X}_j\|}{R}\right)_+ > 1 \\ -2x^3 + 3x^2 & ,x \leq 1 \end{cases} \tag{17}$$

where $(\cdot)_+$ returns a zero for a negative argument. The radius $R(\mathbf{X})$ is determined by the maximum distance of the N_w nearest neighbors of the query point $\mathbf{X}$, as is done in ref 26. The additional parameter S allows reduction of the distance dependence of the localization function; that is, choosing S large will result in $\varsigma_j(\mathbf{X}) \neq 1$ only within a small shell at the boundary of ω_j. In this way, we ensure that the weights are almost purely error based (except for the localization).

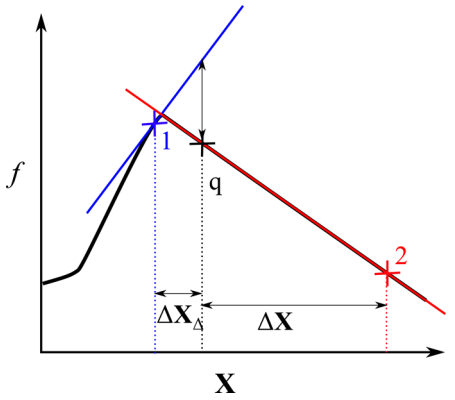

Figure 1. Illustration of the limitation of reaction rate interpolation using pure distance weighting (see text). Given are the data points 1 and 2 with their respective linear Taylor polynomials $Q_1(\mathbf{X})$ (blue line) and $Q_2(\mathbf{X})$ (red line). At the query point $\mathbf{X}_q$, the true function (black) is almost perfectly given by the value of $Q_2(\mathbf{X})$. However, since point 1 lies much closer ($\Delta\mathbf{X}_1 < \Delta\mathbf{X}_2$), it gets a high weight in the distance weighting, leading to a bad representation of the true function at the query point $\mathbf{X}_q$.

What remains is a suitable expression for the error bounding functions $\epsilon_j(\mathbf{X})$. Approximate Taylor polynomials can be bound by[25]

$$\epsilon_j(\mathbf{X}) = \sum_{m=1}^{N_O} D_{j,m} \|\mathbf{X} - \mathbf{X}_j\|^m + D_{j,N_O+1} \|\mathbf{X} - \mathbf{X}_j\|^{N_O+1}, \quad \forall\, \mathbf{X} \in \omega_j \tag{18}$$

Here N_O is the order of the approximate Taylor polynomial; that is, $N_O = 1$ for linear and $N_O = 2$ for quadratic approximations. The last term results from the typical one-order-higher error bound for Taylor polynomials, and the sum terms account for the errors induced by approximate derivatives.[25] The parameters $D_{j,m} \geq 0$ are, without knowing the function $f(\mathbf{X})$, unknown. We therefore estimate them from the existing data, i.e. from the known error of $Q_j(\mathbf{X})$ at the data points within the corresponding cloud ω_j. For every node j, we therefore fit $N_O + 1$ parameters $D_{j,m}$ such that least-squares deviation of the error bound from the known errors is minimized:

$$\min_{D_{j,m}, \forall\, m} \sum_{\mathbf{X}_i \in \omega_j} (\epsilon_j(\mathbf{X}_i) - |Q_j(\mathbf{X}_i) - f_i|)^2 \tag{19}$$

subject to

$$\epsilon_j(\mathbf{X}_i) - |Q_j(\mathbf{X}_i) - f_i| \geq 0, \quad \forall\, \mathbf{X}_i \in \omega_j$$

and $D_{j,m} \geq 0, \forall m$, where the first constraint ensures the error bound property, eq 16, and the second constraint stems from the derivation of eq 18. This procedure includes having to find for each node j those data points which are inside the cloud ω_j. In other words, we have to find those points for which the node j is among the N_w nearest neighbors. This can conveniently be done during the preprocessing when the approximate Taylor

polynomials are constructed, as this involves anyways a nearest neighbor search. The constructed list of inverse nearest neighbors can then be deleted after the $D_{j,m}$ have been determined.

In the Appendix we benchmark the therewith introduced error-based modified Shepard interpolation (EB-MSI) against the previous distance-based variants or third-order Splines using analytical data functions. These tests indicate a superior performance in accurately reproducing regions with strongly nonlinear transitions at simultaneously coarse data resolution, as would be characteristic for gridded $(N_g + 1)$-dimensional 1p-kMC TOF-maps of reactions involving a large number of N_g different gas-phase species.

2.6. Model Systems and Computational Parameters.

As representative showcases for surface reaction chemistry, we will consider CO oxidation at a $RuO_2(110)$ and at a Pd(100) model catalyst. For both systems, we rely on well established 1p-kMC models that have been shown to faithfully reproduce experimental data at lower pressure conditions where heat and mass flow effects are negligible.[17,23,27−29] Specifically, both models employ lattice representations of the active surface including different active site types, and account for all noncorrelated elementary processes that can take place on these lattices: dissociative O adsorption and associative O desorption, unimolecular CO adsorption and desorption, O and CO surface diffusion, as well as Langmuir−Hinshelwood CO + O surface reactions. All rate constants have been determined through DFT and hTST, and detailed accounts of their computation have been given in the original literature.[17,29] The original 1p-kMC model for CO oxidation at Pd(100) was developed to describe the catalytic activity of Pd(100) at lower pressures and concomitantly lower coverages though. For the ambient pressures considered in this work, the model instead predicts coverages that are close to the maximum possible within the model (∼0.5 monolayer). For consistency we therefore employ the O binding energy value of −1.05 eV computed with DFT for this coverage instead of the low-coverage value of −1.25 eV employed in the original work,[29] and replace the generic unity initial sticking coefficients with 0.3 for oxygen adsorption and 0.8 for CO adsorption to reflect corresponding experimental data.[30−32]

Both 1p-kMC models were implemented into and evaluated using the kmos kMC software package.[18] In both models CO oxidation steps are treated as associative desorption processes and CO_2 readsorption is neglected. The steady-state intrinsic TOFs produced by the 1p-kMC simulations therefore only depend on temperature and the partial pressures of CO and O_2; that is, the interpolation task is reduced to a three-dimensional data field. In the case of RuO_2, this data set is the same as already employed and detailed in previous studies focusing on idealized reactor geometries.[6−8] It does not feature overly strong TOF-variations over narrow ranges of gas-phase conditions, which is why already a distance-based modified Shepard interpolation[26] provides a faithful continuous representation. The specific parameters employed in this interpolation are $N_w = 20$, $N_q = 5$, $a_{CO} = 1/6$, $a_{O_2} = 4/15$, and $b_T = 5.1 \times 10^{-5}$.

In comparison the Pd(100) 1p-kMC model yields much more rapid and large activity changes, and is correspondingly more challenging to interpolate reliably. The range of reaction conditions considered is $p_{O_2} \in [10,50]$ mbar, $p_{CO} \in [0.08, 50]$ mbar, and $T \in [500, 650]$ K. Using $a_{CO} = 0.04$, $a_{O_2} = 0.04$, and $b_T = 3.1 \times 10^{-5}$, we initially considered an equidistant data set consisting of 17 points in the O_2 dimension, 65 points in the CO dimension, and 16 points in the temperature dimension. For a better resolution of the rapid change in the TOF at higher CO partial pressures, points on a grid with half the grid spacing have been added, if they where close to this transition, leading to a total of ∼32000 data points. This data field was interpolated with the EB-MSI approach, using $N_w = 35$, $N_q = 100$, and $S = 100$. A two-dimensional cut through the obtained representation is displayed in Figure 2 for constant $p_{O_2} = 30$ mbar and visualizes the mentioned sharp transitions between high and low intrinsic catalytic activity. Similar to the analytic test case described in the Appendix, distance-based modified Shepard interpolation (not shown) always led to oscillations and severe overestimation of the TOF close to these transitions.

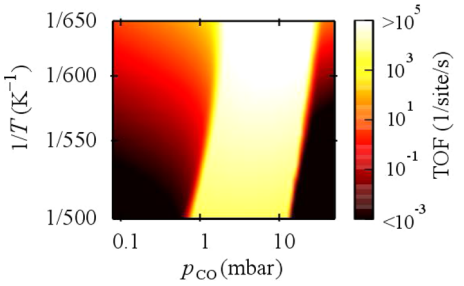

Figure 2. Two-dimensional cut through the intrinsic TOF-map at constant $p_{O_2} = 30$ mbar as obtained by EB-MSI interpolation of 1p-kMC data for the CO oxidation at Pd(100). Note the sharp transitions between regions of high and low catalytic activity, which generally challenge the interpolation of gridded data sets of limited resolution.

Using the continuous intrinsic TOF representations for the boundary conditions, eqs 8 and 9, the resulting reactive CFD simulations were performed with the CatalyticFoam solver.[5] In all CFD simulations, the nonlinear equations were solved using the implicit Euler for the time discretization, and cell centered Gaussian Finite Volumes with linear interpolation for spatial discretization. For the two-dimensional cases, we have used the GMSH mesh generator[33] to generate triangular meshes. In these cases we employed a nonorthogonality correction in the Finite Volume discretization.

3. FLOW SIMULATION RESULTS

In the following we provide several showcases to illustrate the capabilities of the established framework. Even though more generally applicable, we focus here on reactor geometries and flow situations involving flat-faced model catalysts. It is particularly for such catalysts that detailed 1p-kMC models become more generally available, while simultaneously dedicated *in situ* approaches are being developed to provide at best atomic-scale surface characterization of the operating surface.[34] It is within the concomitant aim of a full mechanistic understanding that the effects of flow and surface chemistry need to be most carefully disentangled. The showcases highlight how the coupling of these two aspects generally modifies the observable catalytic function in nontrivial ways. Integrated multiscale simulation approaches such as the present framework are therefore important tools to analyze and understand corresponding *in situ* data or support the development of improved experimental setups.

3.1. Stagnation Flow Reactor. We start to exploit the new possibility to integrate 1p-kMC based surface chemistry into real reactor models by scrutinizing results obtained previously for an ideal stagnation flow reactor.[6,7] A special property of this in general axial-symmetric reactor geometry illustrated in Figure 3 is that, in the limit of large catalyst diameter, the flow problem

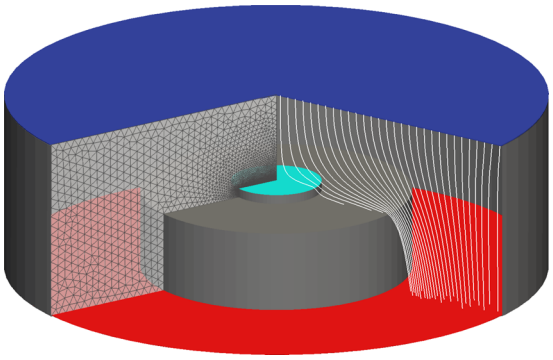

Figure 3. Representation of the considered stagnation flow reactor, featuring the sample holder (gray) at its center. Supported on the sample holder is the single-crystal catalyst with only the top face active (turquois). The gas enters with a uniform velocity field through a sieve-like inlet at the top (blue), streams against the catalyst, and leaves through the outlet at the bottom (red). Typical streamlines for this flow are shown superimposed on the right, while the triangular mesh employed in the CFD simulation is shown on the left.

can effectively be reduced to a one-dimensional problem that describes the velocity, concentration, and temperature profiles in the central region above the catalyst.[9] Within this ideal stagnation flow description, an intriguing bistability with one nonreactive and one highly reactive stationary solution had been obtained for the 1p-kMC CO oxidation at the $RuO_2(110)$ model. This finding is inasmuch interesting, as the 1p-kMC model itself does not show multiple steady states; that is, the observed bistability arises solely from the coupling of gas-phase transport and surface kinetics.[7]

The flat-faced catalyst surface assumed in the stagnation flow geometry, cf. Figure 3, is perfectly suited for single-crystal model catalysts. For reasons of cost or the reduction of reaction heat release, only small diameters are employed in real experiments though. In this respect, it is specifically interesting to evaluate if the full axial-symmetric flow problem with finite catalyst diameter still exhibits the bistability obtained before in the ideal stagnation flow case. We address this with the explicit reactor geometry shown in Figure 3, using dimensions representative of corresponding reactor types:[35,36] The axial-symmetric reactor has a diameter of 6 cm and a height of 2 cm, and features a sample holder (diameter 30 mm; height 9 mm) at its center. The sample holder supports a $RuO_2(110)$ single-crystal catalyst sample with a height of 1 mm and varying diameters. Only the top face of the catalyst is assumed to be reactive. The gas enters at the top through a sieve-like inlet, which ensures a uniform velocity field of 20 cm/s pointing toward the catalyst surface. The computational domain is discretized with a triangular mesh with a minimum grid resolution of 0.05 mm at the catalyst surface and a smooth grading to a maximum grid resolution of 1 mm close to the reactor walls, as illustrated in Figure 3. Assuming isothermal conditions, we specifically focus on gas-phase conditions that fall within the bistability region observed in the ideal solution: T = 600 K, p_{CO} = 1.9 bar, and p_{O_2} = 0.3 bar. The corresponding stationary flow profile is reached by starting with an initial mixture with 99 wt % CO (but the same total pressure) and then a change to the nominal conditions.

Figure 4 summarizes the results obtained for varying catalyst diameter and compares them to the ideal stagnation flow

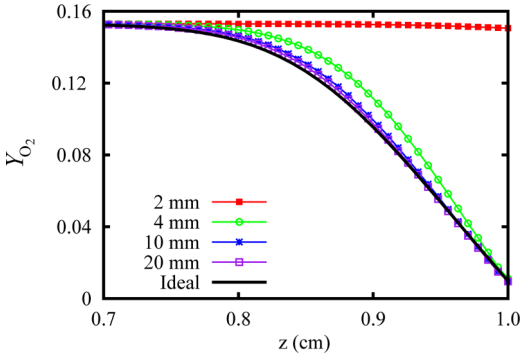

Figure 4. Calculated O_2 mass fraction along the symmetry axis of the stagnation flow reactor shown in Figure 3, where z = 1 cm corresponds to the catalyst surface and z = 0 to the inlet position. For the considered gas-phase conditions (p_{CO} = 1.9 bar, p_{O_2} = 0.3 bar, T = 600 K, inlet velocity of 20 cm/s), the results obtained for large $RuO_2(110)$ catalyst diameters exceeding 1 cm agree with those obtained in the ideal stagnation flow case (black solid line, see text). Due to high catalyst activity, the reactor is in a mass-transfer-limited regime and the mass fraction of the minority O_2 species close to the active surface is significantly reduced. Smaller samples deviate increasingly from the ideal stagnation flow solution. Particularly for the smallest diameter of 2 mm, the active steady state cannot be reached.

solution. The shown O_2 mass fraction along the symmetry axis in the center of the reactor demonstrates that almost perfect agreement with the ideal solution is obtained for catalyst diameters exceeding 1 cm. In this case, the axial-symmetric two-dimensional flow simulation yields an equally active catalyst and a corresponding strong reduction of the minority O_2 mass fraction close to the surface; that is, under these conditions the reactor is in a mass-transfer limited regime.[6,7] For smaller diameters, deviations increase, and particularly for the smallest diameter of 2 mm, the reactive solution is no longer reached. The latter qualitative difference for this catalyst diameter can be rationalized by two aspects, which both lead to larger velocities at the surface: The radial CO_2 concentration gradients induced by the CO_2 drop at the edge of the catalyst are stronger, and at such a small catalyst loading, the sample holder itself replaces the protruding catalyst as the stagnation surface. In this situation, correspondingly strong mass-transfer limitations as in the case of the ideal solution cannot build up. Yet, the latter and their concomitant reduction of the minority O_2 species are indispensably required to bring the partial pressure ratio close to the surface to a regime that leads to the high TOFs of the active state. Small details of the real reactor geometry are therefore critically important for the observable catalytic function, while it is in turn specifically the possibility to explicitly account for these details that now allows us to closely guide experimental approaches that aim to address the predicted bistability.

3.2. Isothermal vs Adiabatic Channel Flow. With the second example we specifically emphasize how subtle features of the intrinsic catalytic activity that are only captured on the level of 1p-kMC simulations carry over to nonintuitive effects at the reactor level. The $RuO_2(110)$ model catalyst surface

exhibits severe oxygen diffusion limitations in its trench-like arrangement of active sites.[17,19,20] Within the 1p-kMC CO oxidation model, these limitations are captured, and in the near-ambient pressure regime, they yield a shift of the partial pressure ratio for which a significant intrinsic catalytic activity is obtained at increasing temperatures. This shift toward higher p_{CO}/p_{O_2} ratios can clearly be seen in the interpolated intrinsic TOF-map shown in Figure 5. In contrast, a mean-field rate

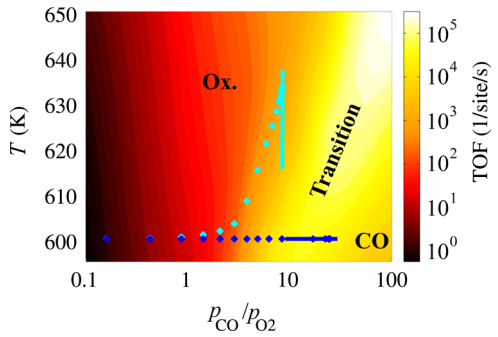

Figure 5. Intrinsic TOF-map for the CO oxidation at $RuO_2(110)$ 1p-kMC model as a function of the partial pressure ratio and temperature for constant total pressure of 5 bar. A rim of highest catalytic activity arises at the transition between an O-poisoned coverage (Ox.) regime in the upper left part of the shown range and a CO-poisoned coverage regime (CO) in the lower right part. Note the tilt of this rim toward higher p_{CO}/p_{O_2} ratios with increasing temperature, that is not obtained by a mean-field rate equation based microkinetic model (see text). Additionally marked with squares is the evolution of the gas-phase conditions at the center of the catalyst within the channel flow reactor after the switch to active feed for the isothermal (blue) and the adiabatic case (turquois). The solid blue and turquoise lines further indicate the finally obtained range of gas-phase reaction conditions over the catalyst surface in the steady state for the isothermal and adiabatic cases, respectively.

equation based microkinetic model would already predict a high TOF at much lower p_{CO}/p_{O_2} ratios, despite using the exact same mechanism and first-principles rate constants.[19]

We illustrate the reactor level consequences of this TOF-feature for a two-dimensional channel flow geometry that we had already employed in earlier work.[20] In this geometry shown in Figure 6, two parallel plates of length 13 cm are placed at a distance of 1 cm. At the inlet, a parabolic Hagen–Poiseuille velocity profile with maximum velocity of 100 cm/s is set, reflecting an unreactive channel flow upstream of the catalyst. The catalyst of length 1 cm and with a height of 1 mm is placed 1 cm downstream of the inlet at the lower plate. Again only the top face of the catalyst is assumed catalytically active. Figure 6 also illustrates the employed mesh representation, which varies in its resolution from 0.25 mm and 1 mm at the inlet and outlet, respectively, down to 0.05 mm at the catalyst surface.

We consider two extreme cases with regard to the dissipation of the released reaction heat: (i) isothermal operation, where reactor walls and catalyst have the same temperature as the gas at the inlet, and (ii) adiabatic operation, where no heat dissipation is allowed into any solid parts of the reactor. In both cases we first bring the system to a steady state for unreactive feed conditions, corresponding to $p_{CO}/p_{O_2} = 0.09$, $p = 5$ bar, and $T = 600$ K. For these conditions, the catalyst is completely inactive, and uniform concentration and temperature profiles are obtained throughout the channel for both the adiabatic and isothermal cases. The inlet mixture is then changed to $p_{CO}/p_{O_2} = 7.3$, that is, to conditions which nominally correspond to high intrinsic catalytic activity (cf. Figure 5). Within 1 s, resolved in 5×10^6 time steps, the system reaches the new steady state. Unexpectedly and as shown in Figure 7, this steady state features a much higher CO_2 concentration above the catalyst surface in the isothermal case. The catalyst is thus markedly more active, even though in the adiabatic case the surface heats up by up to 35 K due to the inefficient heat dissipation into the surrounding gas stream.

The at-first-glance, surprising observation that a hotter catalyst at nominally highly reactive feed conditions exhibits lower catalytic activity can be directly traced back to the TOF topology shown in Figure 5. The mass-transfer limitations that set in already for the initial nominal feed conditions will generally reduce the minority species close to the catalyst surface and therewith expose the catalyst to gas-phase

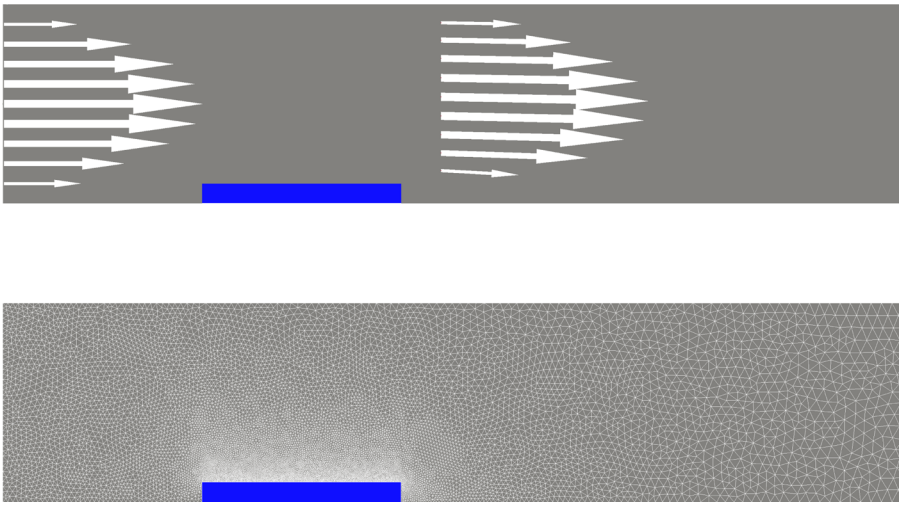

Figure 6. Representation of the considered channel flow geometry, with the catalyst (blue) placed at the bottom plate. The upper panel depicts the velocity profile with the lengths of the vectors proportional to the velocity, and the lower panel shows the employed mesh representation with a resolution as low as 0.05 mm close to the catalyst surface.

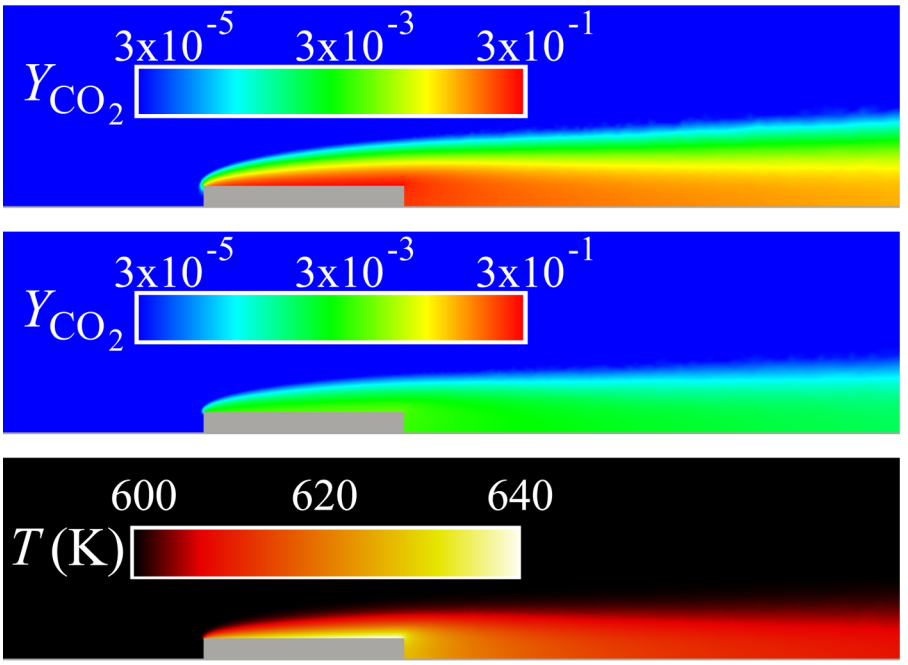

Figure 7. Steady-state CO_2 mass fraction (in logarithmic scale) for the isothermal channel (upper panel) and the adiabatic channel (middle panel), as well as the temperature profile for adiabatic operation (lower panel). Shown are results for a gas-phase feed of p_{CO}/p_{O_2} = 7.3, p = 5 bar, and T = 600 K at the inlet. Although the released reaction heat increases the temperature at the $RuO_2(110)$ catalyst surface by up to 35 K in the adiabatic case, a markedly lower activity is obtained compared to isothermal operation.

conditions corresponding to a further increased p_{CO}/p_{O_2} ratio. As discernible from the intrinsic TOF-map of Figure 5, this brings the system into regions of even higher intrinsic reactivity in the isothermal case. The thereby intensified mass-transfer limitations further increase the p_{CO}/p_{O_2} ratio, and upon approaching steady state, the system successively approaches the highest-activity TOF-rim, as shown in Figure 5. In contrast, in the adiabatic case, any increase in the intrinsic TOF due to an increased partial pressure ratio goes hand in hand with an increase of the surface temperature. With the above-described specific shift of the highest-activity rim toward higher partial pressure ratios at increasing temperatures, this leads to a smaller mutual enhancement of mass-transfer limitations and intrinsic TOF. As a consequence and as shown in Figure 5, the system then eventually settles at the flank of the TOF-rim at a significantly lower steady-state catalytic activity as compared to the isothermal case. With this explanation, the current example thus not only emphasizes again the close coupling of the specifics of the surface kinetics with transport but also furthermore highlights the relevance of heat dissipation channels, which can only be properly accounted for in realistically described reactor geometries.

3.3. Prototypical Reactor for *in Situ* Spectroscopy. The last two examples can still be considered as rather well controlled flow geometries, but they nevertheless exhibited already peculiar couplings between chemistry and transport. With the last example we illustrate that an explicit account of the reactor geometry is even more important for present-day experimental setups for dedicated *in situ* spectroscopies of model catalysts. The design of chambers for the latter task is heavily constrained by the need to place invasive machinery such as pumps or local probes in the immediate vicinity of the catalyst surface.[34] This generally leads to very complex flow profiles, as we exemplify by analyzing the prototypical geometry shown in Figure 8. Without yet including any specific invasive analysis or pumping equipment, the reactor itself consists of a

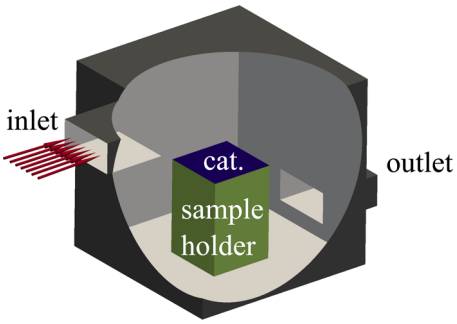

Figure 8. Representation of the reactor geometry considered as prototypical for *in situ* spectroscopic measurements of model catalysts. The gas enters with a uniform velocity at defined temperature at the inlet on the left, streams over the model catalyst surface (blue), and leaves the chamber through the outlet on the right. External heating allows us to control the temperature of catalyst and sample holder (green), while all remaining walls are set to adiabatic boundary conditions.

cube of edge length 3 cm, with a cuboid sample holder with a base of 1 × 1 cm^2 and a height of 1.5 cm mounted at the bottom wall. For simplicity, the catalyst surface is modeled to cover the entire top face of the sample holder. External heating allows us to maintain a constant temperature at both the reactive surface and the side walls of the sample holder, while the remaining reactor walls are assumed to be adiabatic. The gas streams into the reaction chamber through an inlet on the upper left and leaves the chamber through an outlet on the lower right. For the CFD simulations, we exploit the mirror symmetry of the problem, and discretize one-half of the

chamber with a uniform regular cubic mesh. At a resolution of 0.2 mm, this results in 848 000 computational cells.

Considering the CO oxidation on the Pd(100) 1p-kMC model, we focus on a catalyst/sample holder temperature of 600 K and a total pressure of 1 bar. The gas enters at the inlet with a temperature of 300 K, and mass fractions of 0.96, 0.03, and 0.01 for an Ar buffer gas, O_2, and CO, respectively. At a uniform velocity profile of 4 cm/s, this leads to a total flow rate of 120 mL/min through the reactor, which falls within the range characteristic for *in situ* experiments using flow reactors. With such experiments generally focusing on the temperature control of the catalyst, also the large difference in temperature at the inlet and the catalyst surface and sample holder is quite representative. As initial conditions we choose uniform values for all fields in the reaction chamber, employing the values from the inlet (from the outlet for the total pressure). The solution is then advanced with time steps of 5×10^{-5} s until we have reached a total time of 15 s. At this time, the gas in the chamber has—on average—been once or twice exchanged and the system has reached a pseudostationary dynamics in which the relevant flow features are fully established. Not surprising in view of the temperature mismatch of inlet and catalyst, a significant degree of thermoconvection has emerged in this pseudostationary state. Even in the absence of the actual invasive machinery, this leads already to a highly complex flow pattern, which we illustrate in Figure 9. Due to gravity, the

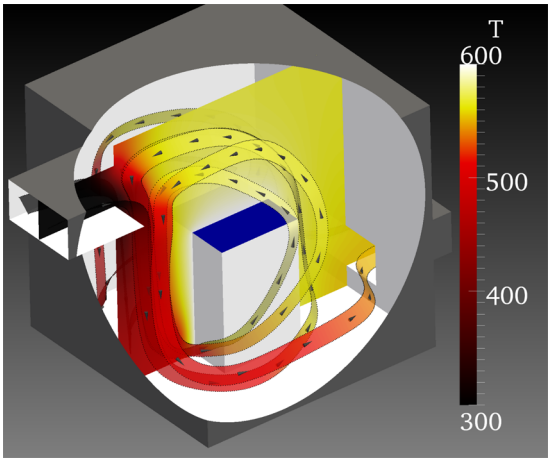

Figure 9. Illustration of the complex stationary flow pattern arising during CO oxidation at Pd(100) inside the reactor. The catalyst and sample holder are maintained at 600 K, while the gas enters at the inlet with 300 K, a total pressure of 1 bar, Ar:CO:O_2 mass fractions of 0.96:0.01:0.03, and a uniform velocity of 4 cm/s. Shown are the temperature distribution at the symmetry plane and along two stream ribbons displaying the gas flow. The black to white color code indicates the temperature $\in [300, 600]$ K both on the ribbons and at the slice. The arrows on the ribbons indicate the streaming direction.

denser gas from the cold inlet drops when entering the reaction chamber and streams toward the outlet along the bottom of the chamber. Once the gas reaches the hot sample holder, it heats up and rises, thereby inducing a vortex, which rotates counterclockwise around the catalyst. For the chosen inlet conditions, the catalyst ends up in a highly reactive state, leading, in fact, within seconds to strong mass-transfer limitations, as apparent from the calculated mass fractions of the minority CO species inside the reactor. However, even without such limitations, i.e. for a potentially less reactive catalyst state, the complex flow pattern would render it impossible to deduce the actual TOFs from a measurement of, for example, the product mass fraction at the outlet. This must be clearly borne in mind when aiming to relate spectro- or microscopic data obtained *in operando* in such chambers to a possible activity of the catalyst.

4. CONCLUSIONS AND OUTLOOK

We have presented a general numerical approach to consider gridded catalytic activity data of complex microkinetic models such as 1p-kMC inside CFD simulations. This allows us to account within one multiscale modeling framework for both the predictive-quality surface kinetics and the heat and mass flow inside an explicitly described reactor geometry. The suitable exploitation of the disparate time scales of surface chemistry and transport in the form of an instantaneous steady-state approximation reduces the actual coupling task to an efficient and reliable interpolation of the gridded activity data. To this end, we have devised an error-based variant of the general modified Shepard method to specifically cope with the abrupt variations of catalytic activity over narrow ranges of gas-phase conditions that are characteristically obtained within 1p-kMC descriptions.

For a given 1p-kMC model, the capabilities and limitations of the resulting approach are correspondingly not governed by the coupling itself, but instead by the actual CFD solver employed. Relying on an interface to the state-of-the-art CatalyticFoam package, the showcases presented in this work demonstrate that this allows us to address realistic reactor geometries of the complexity level, e.g. encountered in *in situ* characterization experiments on model catalysts. A sole notable exception in this context would be *in situ* X-ray photoelectron spectroscopy, where the strong pressure gradients induced by differential pumps placed in the immediate vicinity of the catalyst surface cannot be treated within continuum fluid dynamics. The same reason also presently prevents access to explicitly resolved microporous supports. Still challenging is also the treatment of supported nanocatalysts or polycrystalline surfaces. This has less to do with the fundamental inadequateness of the coupling approach, but rather the practical reason of only limited knowledge about the surface morphology. Even if known, the setup of a reaction mechanism (and the kMC model) and the determination of the corresponding large number of first-principles parameters may become a major task.

For the important class of single-crystal model catalysts or nanoparticle catalysts at planar supports, the presented showcases highlight the intricate coupling of surface chemistry and transport, which generally prevents a clear-cut interpretation of *in situ* characterization data obtained at near-ambient conditions. To a large part this has, of course, to do with the focus on CO oxidation, which is the fruitfly "prototypical" reaction traditionally considered in ultrahigh vacuum and *in situ* model catalyst studies. This facile reaction yields very high conversions and therewith makes mass-transfer limitations almost unavoidable. However, in particular, the details of the heat flow are likely to decisively influence also more selective reactions at lower conversions. Inefficient heat dissipation or external temperature control only over parts of the reactor chamber can lead to significant temperature gradients and therewith to an unknown degree of surface heating and/or thermoconvection. In all such cases, accompanying multiscale simulations of the type and capability presented here will be almost certainly necessary to properly interpret measured data

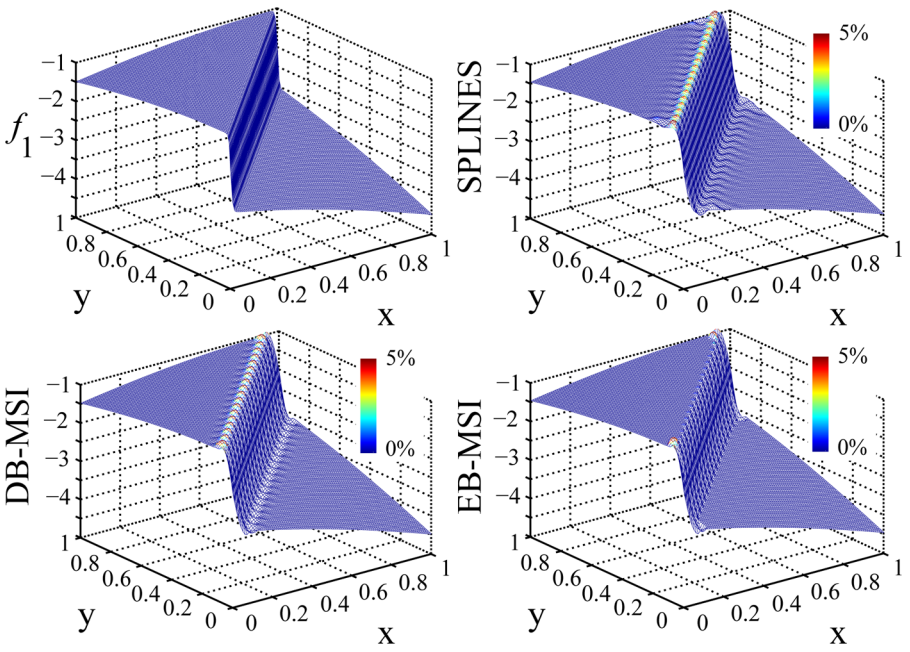

Figure 10. Function f_1 for $u = 200$ (upper left panel) and its approximations obtained by interpolation with Splines (upper right panel), distance-based modified Shepard (DB-MSI, lower left panel), and error-based modified Shepard (EB-MSI, lower right panel). The color code in the three interpolation panels indicates the overestimation of the actual height of the (quasi) discontinuity in percent.

from *in situ* experiments or to design appropriate experimental setups where corresponding effects can be minimized or controlled.

APPENDIX

We benchmark the performance of the error-based modified Shepard interpolation (EB-MSI) using the analytical test function

$$f_1(x, y) = -2\mathrm{sig}(x - y, u) + (1 - \mathrm{sig}(x - y, u))$$
$$(x - y - 4) + \cos(x - y) \qquad (20)$$

with the sigmoid function $\mathrm{sig}(z, u) = (1/(1 + \exp(-uz)))$. In the coordinate $(x - y)$ this function features a transition between otherwise almost linear behavior, whereby the steepness of the transition depends on the parameter u. In particular for large $u \geq 100$, the transition is strongly nonlinear and f_1 features all characteristics of 1p-kMC based TOF-maps. We sample the function at (21×21) equidistant data points in the data range $0 \leq x, y \leq 1$, and therewith create a data field with a resolution typical for high-dimensional 1p-kMC TOF-maps.

Figure 10 compares the performance against interpolation with distance-based modified Shepard interpolation (DB-MSI) as implemented in the ALGLIB library[26] and against third-order Splines. For both Shepard interpolations $N_w = N_q = 8$ and quadratic polynomials were employed. For the chosen large $u = 200$, corresponding to a steep transition, both DB-MSI and Splines have problems in properly representing the transition domain at the given limited grid resolution. In contrast, EB-MSI suppresses artificial oscillations at the transition and thereby prevents spurious overestimation of the function. In flow simulations, particularly the latter features of a reactive boundary condition (oscillations, overestimation) can induce instabilities and hysteresis, and as such, their suppression through the EB-MSI approach is a significant benefit in the present context. Of course, at higher data resolution or smoother transitions corresponding to smaller values of u, all three methods perform equally well, featuring interpolation errors that are negligible for the purpose of interpolating gridded TOF-maps.

AUTHOR INFORMATION

Corresponding Authors

*E-mail: sebastian.matera@ch.tum.de.

*E-mail: matteo.maestri@polimi.it.

Present Address

[§]For S.M.: Freie Universität Berlin, Institut für Mathematik, Arnimallee 6, D-14195 Berlin, Germany.

Notes

The authors declare no competing financial interest.

ACKNOWLEDGMENTS

We gratefully acknowledge generous computing time at the Leibniz Supercomputing Center (Munich, Germany).

REFERENCES

(1) Deutschmann, O., Ed. *Modeling and Simulation of Heterogeneous Catalytic Reactions: From the Molecular Process to the Technical System*; Wiley-VCH: Weinheim, 2013; pp 1−370.

(2) Janardhanan, V. M.; Deutschmann, O. In *Modeling and Simulation of Heterogeneous Catalytic Reactions: From the Molecular Process to the Technical System*; Deutschmann, O., Ed.; Wiley-VCH: Weinheim, 2013; pp 251−282.

(3) Sabbe, M. K.; Reyniers, M.-F.; Reuter, K. *Catal. Sci. Technol.* **2012**, *2*, 2010−2024.

(4) Reuter, K. In *Modeling and Simulation of Heterogeneous Catalytic Reactions: From the Molecular Process to the Technical System*; Deutschmann, O., Ed.; Wiley-VCH: Weinheim, 2013; pp 71−112.

(5) Maestri, M.; Cuoci, A. *Chem. Eng. Sci.* **2013**, *96*, 106−117.

(6) Matera, S.; Reuter, K. *Catal. Lett.* **2009**, *133*, 156−159.

(7) Matera, S.; Reuter, K. *Phys. Rev. B* **2010**, *82*, 085446.

(8) Matera, S.; Reuter, K. *J. Catal.* **2012**, *295*, 261−268.

(9) Kee, R. J.; Coltrin, M. E.; Glarborg, P. *Chemically reacting flow: theory and practice*; John Wiley & Sons: 2005.
(10) Chapman, S.; Cowling, T. G. *The mathematical theory of non-uniform gases: an account of the kinetic theory of viscosity, thermal conduction and diffusion in gases*, 3rd ed.; Cambridge University Press: 1970.
(11) Coffee, T.; Heimerl, J. *Combust. Flame* **1981**, *43*, 273−289.
(12) Vlachos, D. G. *AIChE J.* **1997**, *43*, 3031−3041.
(13) Kissel-Osterrieder, R.; Behrendt, F.; Warnatz, J. Detailed modeling of the oxidation of CO on platinum: A Monte-Carlo model; Symposium (International) on Combustion; 1998; pp 2267−2274.
(14) Majumder, D.; Broadbelt, L. J. *AIChE J.* **2006**, *52*, 4214−4228.
(15) Schaefer, C.; Jansen, A. P. *J. Chem. Phys.* **2013**, *138*, 054102.
(16) Neurock, M.; Hansen, E. W. *Comput. Chem. Eng.* **1998**, *22*, S1045−S1060.
(17) Reuter, K.; Scheffler, M. *Phys. Rev. B* **2006**, *73*, 045433.
(18) Hoffmann, M. J.; Matera, S.; Reuter, K. *Comput. Phys. Commun.* **2014**, *185*, 2138−2150.
(19) Temel, B.; Meskine, H.; Reuter, K.; Scheffler, M.; Metiu, H. *J. Chem. Phys.* **2007**, *126*, 204711.
(20) Matera, S.; Meskine, H.; Reuter, K. *J. Chem. Phys.* **2011**, *134*, 064713.
(21) Meskine, H.; Matera, S.; Scheffler, M.; Reuter, K.; Metiu, H. *Surf. Sci.* **2009**, *603*, 1724−1730.
(22) Reuter, K.; Scheffler, M. *Phys. Rev. Lett.* **2003**, *90*, 046103.
(23) Reuter, K.; Frenkel, D.; Scheffler, M. *Phys. Rev. Lett.* **2004**, *93*, 116105.
(24) Renka, R. J. *ACM Trans. Math. Software (TOMS)* **1988**, *14*, 139−148.
(25) Zuppa, C. *Appl. Numer. Math.* **2004**, *49*, 245−259.
(26) Bochkanov, S. "ALGLIB"; www.alglib.net.
(27) Rieger, M.; Rogal, J.; Reuter, K. *Phys. Rev. Lett.* **2008**, *100*, 016105.
(28) Blomberg, S.; Hoffmann, M. J.; Gustafson, J.; Martin, N. M.; Fernandes, V. R.; Borg, A.; Liu, Z.; Chang, R.; Matera, S.; Reuter, K.; Lundgren, E. *Phys. Rev. Lett.* **2013**, *110*, 117601.
(29) Hoffmann, M. J.; Reuter, K. *Top. Catal.* **2014**, *57*, 159−170.
(30) Orent, T. W.; Bader, S. D. *Surf. Sci.* **1982**, *115*, 323−334.
(31) Stuve, E. M.; Madix, R. J.; Brundle, C. R. *Surf. Sci.* **1984**, *146*, 155−178.
(32) Yeo, Y. Y.; Vattuone, L.; King, D. A. *J. Chem. Phys.* **1997**, *106*, 392−401.
(33) Geuzaine, C.; Remacle, J.-F. *Int. J. Numer. Meth. Eng.* **2009**, *79*, 1309−1331.
(34) Stierle, A.; Molenbroek, A. M. *MRS Bull.* **2007**, *32*, 1001−1009.
(35) Kissel-Osterrieder, R.; Behrendt, F.; Warnatz, J.; Metka, U.; Volpp, H.-R.; Wolfrum, J. *Proc. Combust. Inst.* **2000**, *28*, 1341−1348.
(36) McGuire, N. E.; Sullivan, N. P.; Deutschmann, O.; Zhu, H.; Kee, R. J. *Appl. Catal., A* **2011**, *394*, 257−265.